



# Fatigue-constrained gradient-based design optimization of main bearing–shaft systems for floating wind turbine drivetrains

Vasudev Gupta<sup>1</sup> and Amir R. Nejad<sup>1</sup>

<sup>1</sup>Department of Marine Technology, NTNU, Professor JHL Vogts veg 1a, 7052 Trondheim, Norway

**Correspondence:** Vasudev Gupta (vasudev.gupta@ntnu.com)

**Abstract.** Floating offshore wind turbines have significant potential for economical and environmentally-efficient solutions for energy production. However, current state-of-the-art witnesses a lack of integrated analysis and optimization of these large, dynamically-coupled complex engineering machines and their critical sub-systems, such as the drivetrain, with research and experience still in their infancy. The aim of the paper is to facilitate efficient and holistic gradient-based multi-disciplinary constraint optimization of drivetrains by exploiting numerical models with varied fidelity-levels. This is illustrated through a constraint optimization of the main-shaft assembly, which includes critical fatigue-limit constraints of main-bearings, bridging design load case-based load spectra reduction with analytically-differentiable damage equivalent loads in contrast to conventional non-smooth bin-counting. The importance of fatigue as a design driver is shown by comparison to only static structural design. The proposed methodology is implemented as a modular extension within the open-source WISDEM-WEIS framework based on OpenMDAO, enabling efficient integration into existing multidisciplinary system-level wind turbine design workflows.

## 1 Introduction

### 1.1 Multidisciplinary optimization of floating wind

Wind turbines (WTs) are inherently multi-disciplinary coupled engineering systems, that must withstand extreme stochastic environmental conditions (ECs), satisfy relevant mechanical constraints while producing the highest possible energy at the lowest possible cost. Such are a difficult class of problems to solve, challenging the wind energy and design-optimization state-of-the-art (SoA).

The wind energy community recognises that the current industrial practice of optimizing each component decoupled from the others and sequentially leads to suboptimal design, sometimes being even inconceivable from a system-level perspective (Perez-Moreno et al. (2016); Veers (2019)). Moreover, several research studies (Jasa et al. (2022); Sethuraman et al.; Dykes et al.) give evidence to an optimal consequence when disciplines are integrated and optimized simultaneously for a technical-economic-safety objective.



Therefore, the need to exploit the multidisciplinary nature of WT and to shift to a multidisciplinary design, analysis and optimization (MDAO) basis (Martins and Ning (2022)) contains a huge opportunity for wind energy systems - a science that is still in its infancy.

## 1.2 The need for reliable and optimized drivetrains

The potential of offshore wind cost reduction is high (Musial et al. (2022)), with economics projected to decrease further between 2021-2030. Trends in industrial applications and research literature show that there is not yet a consensus on the optimal drivetrain (DT) design and technology for floating offshore wind turbine (FOWT) applications.

Drivetrains significantly influence the operational reliability and availability of WTs. The unique and harsh operational conditions (OCs) - unsteady loads, high torque variations, axial/thrust loading, parasitic non-torque loads (NLTs), slow rotational speeds (rpm) - that they undergo make their premature failure rates, long downtimes and repair/replacement costs a concern for the wind industry (Nejad (2018); Veers (2019); Wenske (2022); Nejad et al. (2022); Dao et al. (2019)).

With regard to main bearings (MBs), Hart et al. (2023) recently investigated a large dataset of 7,707 WTs and documented significant signs of premature failure, with the locating (thrust-carrying) bearing being the vast majority, and their life largely deviating from standard-based estimations: 10% failure in 10.5 years. At 20 years design life, predicted failure rate was 22-25%. Literature (Chovan and Fierro (2021); Guo et al. (2015a); Wenske (2022); Link et al. (2011)) reasons that in large (multi-MW) WTs, even under normal OCs, unfavourably high axial-to-radial load ratios ( $F_{ax}/F_{rad}$ ) cause unequal load sharing between roller rows of flexible MB setups. Consequently, NLTs and axial displacements enter the gearbox (GB), causing unequal load sharing between planet bearings and meshing gears, that enter into deteriorating regimes. A recent NLR report shows that, of the most prevalent GB failures on onshore WTs, 76.2% are due to GB bearings (Veers (2019)). The GB is also one of the most expensive and heaviest components of a WT-DT. Overall, these phenomenon reduce the reliability and life of the entire DT (Chovan and Fierro (2021); Wenske (2022)).

The current state-of-the-art review concludes that bearings are critical reliability drivers in wind energy, especially offshore wind.

## 1.3 Drivetrain multi-disciplinary design optimization

Novel DT designs for large WTs involve a complex and collaborative process, meeting several technical requirements simultaneously.

Current SoA WT DT analysis is seen to exploit sequential design loops, treating bearings using static load checks with decoupled  $L_{10}$ -life post-processing, and exploiting expensive genetic algorithms for DT component design. In general, design criteria involving structural dynamics and fatigue damage are rarely seen in floating offshore wind turbine (FOWT) optimization, (Patryniak et al. (2022)).

Detailed DT design fully-coupled with efficient gradient-based optimization (GBO) and inclusion of critical fatigue metrics within the system-scope is yet to be seen in wind energy research and industry, which has significant potential for novel so-



lutions: high energy production at increased reliability and lower costs (Wenske (2022); Sethuraman et al.; Guo et al. (2017); Hart et al. (2022)).

60 The present research aims to elucidate on an important topic: **the lack of integration and details of drivetrain design in aero-elastic analyses and system-level FOWT optimization.**

#### 1.4 Numerical frameworks

To enable drivetrain MDAO within the system-scope, the present paper exploits WISDEM, a comprehensive WT system engineering MDAO framework developed by NLR (2026)<sup>1</sup>, which codifies physics-based computational and empirical models  
65 for WT component optimization and cost estimation. WISDEM's key benefits lies in its computational efficiency – inexpensive and fast – to perform steady-state system-level techno-economic (LCOE, AEP) MDAO, conduct preliminary sensitivity studies between coupled components, and quickly access performance trade-offs between potentially viable designs.

However, in light of drivetrain analysis, WISDEM's current module (DrivetrainSE) lacks detail and is insufficient to optimize critical component, falling behind the current industry's performance capabilities. Moreover, its workflows focuses  
70 on sizing and cost, but critical metrics such as fatigue-based reliability and safety margins at the component level (e.g. bearings) are not yet integrated. Given WISDEM's benefits, this creates a gap for the wind energy research and development industry.

#### 1.5 Objective and novelty of the work

The purpose of this study is to fill this gap by introducing detailed bottom-up physics-based drivetrain optimisation within WISDEM-DrivetrainSE through

- 75 1. targeting high impact and critical drivetrain components (e.g. MBs) through coupling between geometry design variables and fatigue safety factors directly in optimization to significantly improve drivetrain design robustness,
2. bridging of design load case (DLC)-based operating-load variable-speed spectra reduction with analytical damage equivalent load (DEL) for bearing fatigue,
3. integration within an efficient GBO framework,
- 80 4. scalable and industry-relevant gradient-consistent drivetrain multi-disciplinary optimization (and integration into MDAO workflow, eg. the openMDAO framework).

Such would enable further research on:

1. drivetrain optimization as a component within the wider WT system-scope.
2. coupled dynamics between turbine components, especially interactions of floating substructure (platform motions), sea  
85 states, drivetrain (loads) and control strategy on large FOWTs.

<sup>1</sup>National Laboratory of the Rockies; formerly the National Renewable Energy Laboratory (NREL)

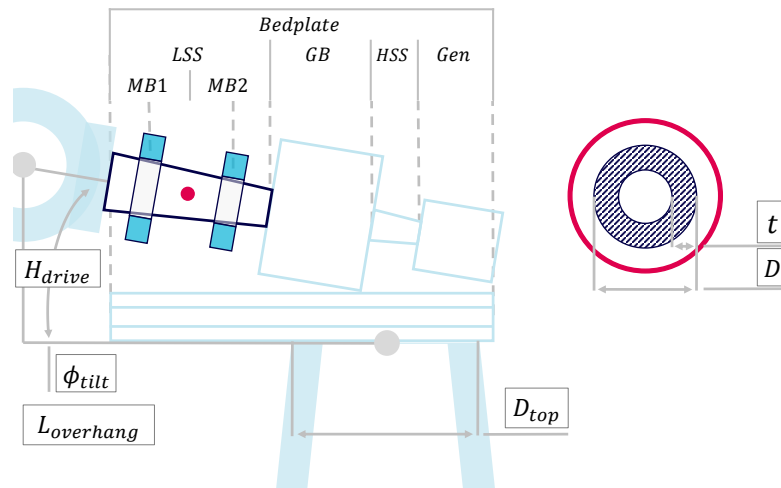


**Figure 1.** Geared Drivetrain Layout for the Made4Wind 15MW

ultimately enhance insights into system-level interactions.

The use case scenario is the IEA-15MW floating reference WT supported on Acciona's CT-bos tension leg platform (TLP) (Sect.A).

### 1.5.1 Scope of the work

90 The paper presents a practical design optimization methodology for the drivetrain components that are first in line in the load path from the aerodynamic rotor blades, namely the main-shaft assembly (MSA; Fig.1), comprising the main shaft (conical, hollow and of steel material (Tab.B2)) and the two main bearings, which support the former, the rotor assembly (hub and rotor blades) and the first-stage GB carrier, Fig. 2.

Due to high reliability requirements for large-FOWT DTs, as well as observations from recent field tests, there is a shift in  
95 focus from flexible to rigid DT configurations utilizing preloaded moment-reacting tapered roller bearings (TRBs) with high contact angles as MBs and first stage planet carrier bearings (Chovan and Fierro (2021); Guo et al. (2015a); Wenske (2022); Link et al. (2011)). Therefore, the selected MB configuration is MB1 being floating, reacting to radial loads (e.g. CRB), while MB2 being fixed/locating, reacting to axial, radial and part of bending (tilting) moment loads (e.g. double-row TRB or TRB2). Such moment-reacting (MR) bearings provide angular stiffness and can transmit bending moments through the rolling-element  
100 contact.

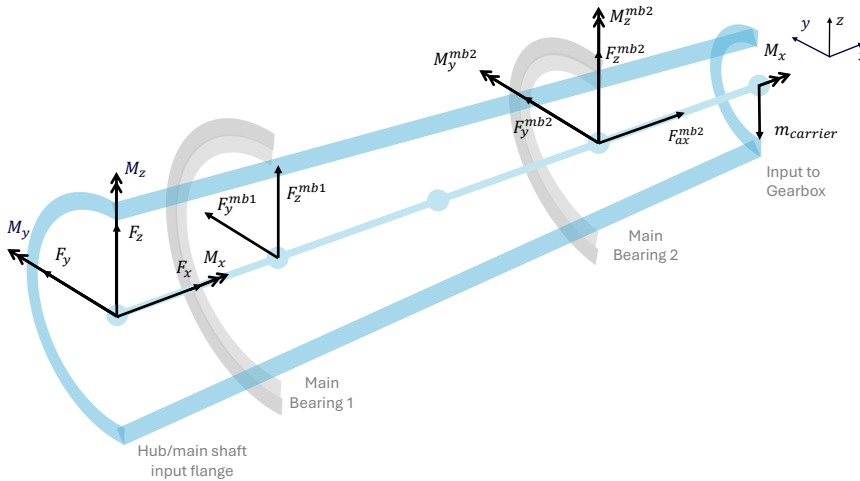


**Figure 2.** Main-shaft assembly (MSA) with respective component loads

## 2 Methodology

### 2.1 Initial design and load cases (DLCs)

This work employs the conventional de-coupled (or 2-step) global-local approach for drivetrain analysis assuming fixed hub loads throughout.

105 To initiate the turbine's design optimization process, some representative (hub) loads are required. The loads acting on the turbine (and its structural components) dictate its sizing which must satisfy the relevant limit stress utilizations and fatigue constraints.

To this end, an initial global FOWT model – representative of the Made4Wind 15MW with a medium-speed 3-stage planetary geared drivetrain, standard floating tower (Allen et al. (2020)) and Acciona's TLP substructure – was created in the aero-hydro-  
110 servo-elastic simulation software `openFAST` to facilitate IEC DLC simulation and loads extraction.

The respective aerodynamic hub load channels extracted from `openFAST` outputs are listed in Tab. 1. The coordinate system is centred at the main shaft-hub interface, non-rotating, and aligned with the tilted low-speed shaft (LSS) (as in A.3, dnv (2016)).

#### 2.1.1 ULS: Steady-state extreme loads

115 Ultimate limit state (ULS) criterion defines a design based on the ability to withstand long-term extreme-occurring loads for a given lifetime, which can be estimated using either of the following 2 methods:

1. Probabilistic extrapolation of loads from DLC with normal operating condition.
2. Maximum occurring loads of DLCs with extreme operating conditions.

The second method, similar to the IEA 15MW turbine reports (Gaertner et al. (2020); Allen et al. (2020)), is used in this study and is described as follows:

120 A selected subset of IEC DLCs – defining normal and extreme environmental conditions, start-up, shutdown, emergency  
 stop and yaw-misalignment – were analysed, wherein the maximum rotor-hub loads were extracted and compared across the  
 DLCs. It was observed that DLC 5.1 (Emergency stop) resulted in the largest overall rotor-main shaft torque and bending  
 moments, which are design drivers for the sizing of drivetrain components, eg. the GB and MSA respectively. Moreover, DLC  
 3.2 (Extreme gust) resulted in the highest axial/thrust loads, which are critical for the design and operation of MBs or MSA.  
 125 Therefore, these maxima values were selected and are presented in Tab.2.

### 2.1.2 FLS: Transient full DLC load matrix

Fatigue limit state (FLS) criterion defines a design based on the ability to withstand fatigue loads (cyclic or repeated loading) during the design lifetime of the component.

130 From aero-elastic simulations of DLC 1.2, the 6-DOF hub forces and moments time series, respectively, acting on the hub flange-main shaft interface were extracted; denoted  $F_*$  and  $M_*$ , Tab.1 and Fig.3.

These raw hub loads time series are piped directly into the new analytical main bearing component within `DrivetrainSE` to formulate fatigue life constraints, as described in the Sect.2.2.

In the following, index  $j$  defines the wind speed bin (eg. [1, 2, ..., 10]), while  $i$  defines the time step instance (eg. [1, 2, ..., 72000]).

**Table 1.** Main shaft hub loads extracted from respective `openFAST` channels, at 20Hz sampling frequency (or step size  $\Delta t = 0.05s$ ).

Notation	Load	Channel	Shape
$F_x$	Thrust	RotThrust	array[72000, 10]
$F_y$	Shear	LSShftFys	array[72000, 10]
$F_z$	Shear	LSShftFzs	array[72000, 10]
$M_x$	Torque	LSShftTq	array[72000, 10]
$M_y$	Pitching	LSSTipMys	array[72000, 10]
$M_z$	Yawing	LSSTipMzs	array[72000, 10]

**Table 2.** ULS hub loads for drivetrain design optimization

Load	$x$	$y$	$z$	units
$F_*^{max}$	5.39	1.36	5.57	MN
$M_*^{max}$	52.51	107.46	99.48	MNm

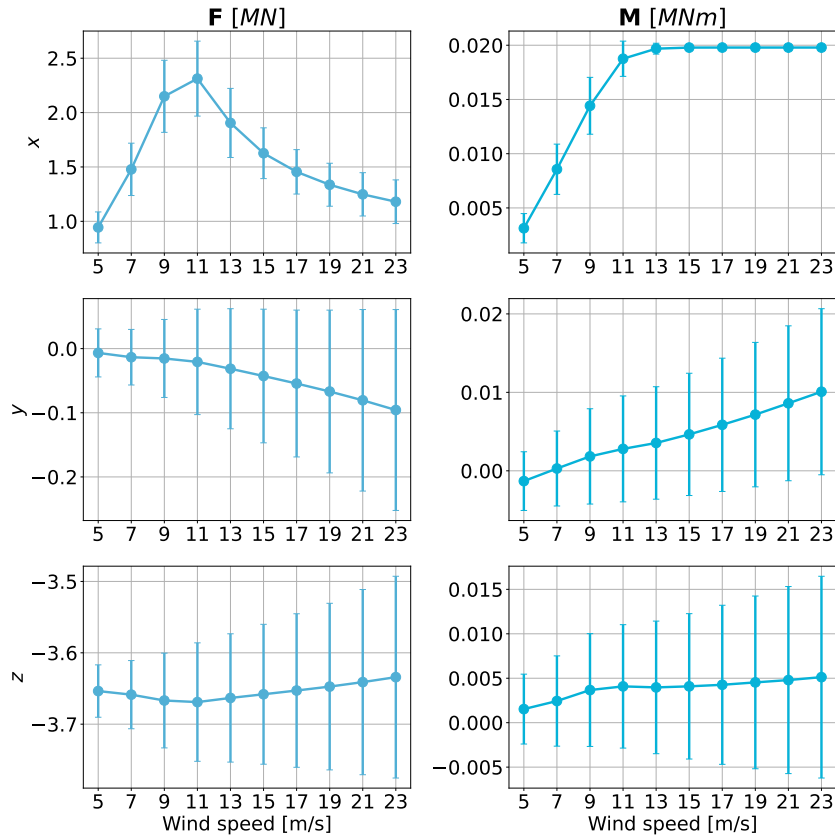


**Figure 3.** Mean and standard deviation of hub/main-shaft loads; **F**-forces and **M**-moments, in  $x, y, z$ -directions.

## 135 2.2 A Fast and Representative Model for Suspension Setups with Moment-Reacting MB2

In the following, a new numerical methodology is devised that enables fatigue limit state (FLS) bearing constraint in an efficient and modular manner for holistic design optimization and propels MDAO studies on wind turbine drivetrains. Based on the MDAO framework `openMDAO` and supplemented in `DrivetrainSE`, it overcomes the latter's limitation of steady-state extreme-loads (ULS) driven analysis and design for drivetrain configuration and components.

140 Guo et al. (2017): "This analysis is driven by extreme loads and does not consider fatigue. Thus, the effects of configuration choices on reliability and serviceability are not captured."

Several studies, such as early NLR drivetrains Guo et al. (2015b)), formulate the analytical low-fidelity load equations assuming no moment-reaction on the locating bearing – only valid for non-moment reacting (non-MR) bearings such as SRBs, CRBs etc. – in order to render a statically-determinate model which can be solved using closed-form equations (Eq.1 and 2 for



145 MB1 and MB2 respectively).

With

$$x_3 = (L_{h1} + L_{12})$$

$$g_x = g \sin(\phi)$$

150  $g_y = 0.0$

$$g_z = -g \cos(\phi)$$

MB1 reactions:

using  $\sum \mathbf{M}^{mb2} = \mathbf{0}$  : (1)

$$\mathbf{F}_{ax}^{mb1} = \mathbf{0}$$

155  $\mathbf{F}_y^{mb1} = \frac{\mathbf{M}_z - \mathbf{F}_y x_3}{L_{12}}$

$$\mathbf{F}_z^{mb1} = \frac{-\mathbf{M}_y - \mathbf{F}_z x_3 + (m_{carrier} g_z) \delta}{L_{12}}$$

MB2 reactions:

using  $\sum \mathbf{F} = \mathbf{0}$  : (2)

$$\mathbf{F}_{ax}^{mb2} = |-\mathbf{F}_x - (m_{carrier} g_x)|$$

160  $\mathbf{F}_y^{mb2} = (-\mathbf{F}_y - \mathbf{F}_y^{mb1})$

$$\mathbf{F}_z^{mb2} = -\mathbf{F}_z - \mathbf{F}_z^{mb1} + (m_{carrier} g_z)$$

On the other hand, mid-fidelity beam models, such as OpenFAST-ElastoDyn as in Liverud Krathe et al. (2025) or the structural solver pyFrame3DD, could be used to calculate the bearing forces and moments. However such methods are computationally too expensive for FLS constraint evaluation of the entire DLC matrix (size  $[72\ 000 \times 10]$ ) in every iteration of a  
 165 gradient-based optimizer.

The application of the above (conventional) analytical formulation for non-MR bearings (e.g. SRB; Eqs.1, 2) to those that physically reacts to moments (e.g. TRB2) was challenged by Stirling et al. (2021) where they showed, for a single-main-bearing (SMB) configuration, that such a formulation highly overestimates the bearing reactions ( $\mathbf{F}$ ) and proposed a torsional-stiffness-  
 170 based analytical moment-reacting (MR) model for such MR bearings, where the stiffness was calculated using a FE bearing model.

Extending their study for the double main-bearing configuration (DMB), similar results are found when bearing reactions are compared between pyFrame3DD structural solver's solution (with a moment-reacting MB2) and the conventional analytical formulation: Fig.4. At magnitudes of MN and MNm, these differences, especially in the radial reactions ( $F_{rad}$ ), exponentially

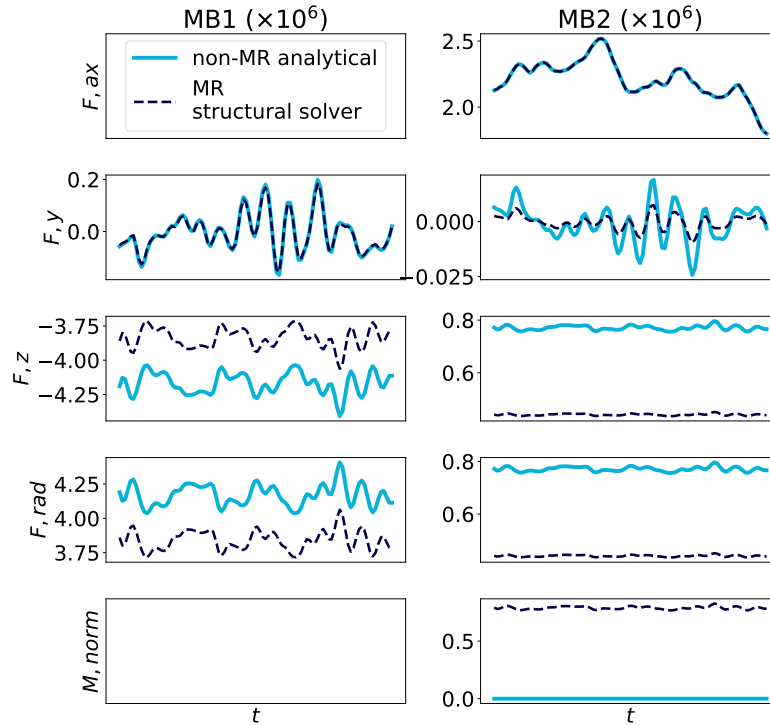


**Figure 4.** Bearing reactions comparison: pyFrame3DD with a moment-reacting MB2, and the conventional analytical formulation without a moment-reacting MB2

175 worsen the fatigue life (to the power of  $p = 10/3$ ; Eq.25), hence requiring proportionally higher dynamic load capacities ( $C$ ), but at the cost of higher bearing diameters and masses (Tab.3) to satisfy the fatigue constraints.

Double-main bearing model with moment-reacting MB2:

To this end, this work presents a **closed-form main bearing loads model** as follows, where the axially locating MB2 reacts to moments ( $M_*^{mb2}$ ) via the torsional spring ( $k_\theta$ ), through the relation  $M_*^{mb2} = k_{**} \cdot \theta_*$ , in the y- and z-directions and where  $\theta$  is the slope/beam's cross-sectional rotation at the MB2-node. The relation is found through the Euler-Bernoulli (EB) beam (moment-slope) equation applied between the main-bearing span ( $L_{12}$ ) with boundary conditions of 0-deflection at the MBs.

1. The EB-beam is assumed between the 2 MB-span (denoted A-B, Fig.5) to derive the slope ( $\theta_B$ ) relation with respect to forces and moments.

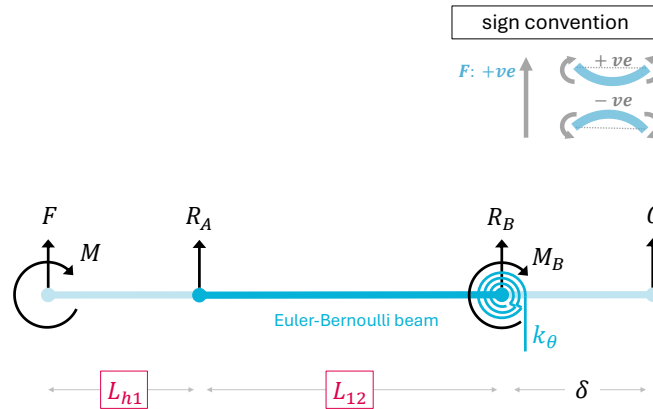


**Figure 5.** MSA with moment-reacting MB2, bearing-span modelled as EB-beam; in each plane

185 2. The full 2-bearing-shaft system with moment-reacting MB2 is reformulated, to derive bearing reaction forces and moments.

### 2.2.1 Slope at MB2 from first principles

Consider the shaft span between bearings *A* and *B*, of length  $L_{12}$ , modelled as an Euler–Bernoulli beam with constant flexural rigidity  $EI$ .

190 Let:

- $x = 0$  at bearing *A* (CRB),
- $x = L_{12}$  at bearing *B* (DTRB),
- $R_A$  and  $R_B$  be the reactions (assumed +ve, vertical).

Since the left bearing (CRB) does not support moment,

195  $M(0) = 0.$  (3)

**Internal Bending Moment:** For a section at distance  $x$  from *A*, the only internal contribution is due to  $R_A$ :

$$M(x) = R_A x, \quad 0 < x < L_{12}. \quad (4)$$

**Beam Equation:** From Euler–Bernoulli beam theory (and substituting  $M(x) = R_A x$ ),

$$EI w''(x) := M(x) = R_A x. \quad (5)$$



200 **First Integration (Slope):** Integrating once:

$$EI w'(x) = \int R_A x dx = \frac{R_A x^2}{2} + C_1. \quad (6)$$

**Second Integration (Deflection):** Integrating again:

$$EI w(x) = \int \left( \frac{R_A x^2}{2} + C_1 \right) dx = \frac{R_A x^3}{6} + C_1 x + C_2. \quad (7)$$

**Boundary Conditions (Assumed)**

205 At  $x = 0$  (bearing  $A$ ), deflection is zero:

$$w(0) = 0 \Rightarrow C_2 = 0. \quad (8)$$

At  $x = L_{12}$  (bearing  $B$ ), deflection is also zero:

$$w(L_{12}) = 0. \quad (9)$$

Substituting:

$$210 \frac{R_A L_{12}^3}{6} + C_1 L_{12} = 0, \quad (10)$$

which gives

$$C_1 = -\frac{R_A L_{12}^2}{6}. \quad (11)$$

**Slope at Bearing  $B$ :** The slope expression is

$$EI w'(x) = \frac{R_A x^2}{2} - \frac{R_A L_{12}^2}{6}. \quad (12)$$

215 Evaluating at  $x = L_{12}$ :

$$EI \theta_B = \frac{R_A L_{12}^2}{2} - \frac{R_A L_{12}^2}{6} \quad (13)$$

$$= \frac{R_A L_{12}^2}{3}. \quad (14)$$

**Compatibility Relation:** Therefore, the rotation at the right bearing is:

$$\theta_B = \frac{R_A L_{12}^2}{3EI} \quad (15)$$

220 **Bearing Constitutive Relation:** The moment at the right bearing is:

$$M_B = k_\theta \theta_B$$

$$M_B = \frac{k_\theta R_A L_{12}^2}{3EI} \quad (16)$$

$$= R_A \cdot \lambda_L$$

where,

$$225 \lambda_L = \frac{k_\theta L_{12}^2}{3EI} = \lambda \cdot L_{12} \quad (17)$$



$k_\theta$  is the moment-reacting bearing's torsional spring constant (in this plane), and  $\lambda_L$  is termed the compatibility term, representing the ratio of bearing rotational stiffness to the shaft bending stiffness.

To this end, the statically-indeterminate equations are now complete (with equal known-loads and unknown-reactions) to render bearing loads using shear force and bending moment equilibrium.

### 230 2.2.2 DMB-shaft model with MR-MB2

Consider, in each plane, a shaft supported by two bearings, with the concentrated forces and moments, as shown in Fig.5, with unknown reactions:  $R_A$ ,  $R_B$ ,  $M_B$ .

Using singularity functions (Budynas et al. (2021)) the shaft's shear force and bending moment equations can be determined.

#### 235 Global Equilibrium (involving only statics):

Denoting  $L = L_{h1} + L_{12} + \delta$ ,

Vertical Force Equilibrium: noting that the shear force outside the MSA should be zero i.e.  $V(L^+) = 0$ :

$$F + R_A + R_B + G = 0 \tag{18}$$

240 or

$$\boxed{R_B = -G - F - R_A} \tag{19}$$

Moment Equilibrium: noting that the bending moment outside the MSA should be zero i.e.  $M(L^+) = 0$ ,

$$M + FL + R_A(L - L_{h1}) + R_B\delta + M_B = 0 \tag{20}$$

Substituting Eq.16 and Eq.19 in Eq.20, and collecting terms in  $R_A$  we get,

$$245 \quad \boxed{R_A = \frac{-M - Fx_3 + G\delta}{L_{12}(1 + \lambda)}} \tag{21}$$

defining the numerator as C,

$$C = -M - Fx_3 + G\delta$$

$$\text{then, } R_A = \frac{C}{L_{12}(1 + \lambda)}$$

#### Limiting Cases:

- 250
1. Case:  $k_\theta = 0$  (No Moment Resistance):  $R_B = \frac{C}{L_{12}}$ . The system reduces to a statically determinate beam (simply supported result).
  2. Case:  $k_\theta \rightarrow \infty$  (Rigid Moment Support): The denominator grows large and the system approaches fixed-end beam behaviour at bearing B.

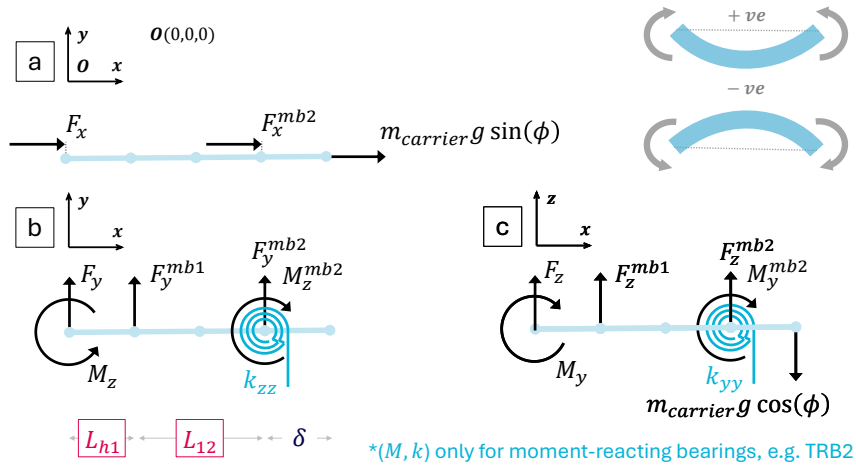


**Figure 6.** Free-body diagram of main-shaft static equilibrium in the local (hub) coordinate system;  
 a: x-plane, b: yx-plane, c: zx-plane; top-right: bending moment convention.

### 2.2.3 Solving for each plane

255 As shown in Fig.6, when the planar equation system from Sect.2.2.2 is solved in the:

- b-plane:  $R_A = \mathbf{F}_y^{mb1}$ ,  $R_B = \mathbf{F}_y^{mb2}$ , and  $M_B = \mathbf{M}_z^{mb2}$ .
- c-plane:  $R_A = \mathbf{F}_z^{mb1}$ ,  $R_B = \mathbf{F}_z^{mb2}$ , and  $M_B = \mathbf{M}_y^{mb2}$ .
- a-plane:  $\mathbf{F}_x^{mb1} = 0$  and  $\mathbf{F}_x^{mb2} = |-\mathbf{F}_x - (m_{carrier} g \sin \phi)|$

with bearing axial ( $\mathbf{F}_x$ ) and radial ( $\mathbf{F}_y$ ,  $\mathbf{F}_z$ ) loads calculated for both bearings.

260 Thereafter, radial loads  $\mathbf{F}_{rad}$  are accumulated as follows:

$$\mathbf{F}_{rad}^* = \sqrt{(\mathbf{F}_y^*)^2 + (\mathbf{F}_z^*)^2}$$

Also, the absolute value operation of the axial force on the locating bearing (MB2) is noted from the above implementation:

$$\mathbf{F}_x^{mb2} = |\dots| = \text{abs}(\dots).$$

The locating bearing always reacts to the magnitude of axial force, regardless of sign. The sign is relevant for internal stress  
 265 direction, but  $\mathbf{P}$  (equivalent bearing load) is always positive in life/fatigue calculations. In other words, whether axial tension  
 or compression, the bearing ‘reacts’ to the load regardless. Therefore,  $|\dots|$  is physically consistent with bearing reactions, as  
 well as gradient calculations because  $\mathbf{F}_x^{mb2}$  is independent of the design variables (its partial derivative is 0).

The resulting bearing reactions using this formulation are validated in Sect.4.1.



## 270 2.3 Bearing Fatigue-life Constraints

### 2.3.1 Empirical relations of bearing properties and bore diameter

The variation of bearing properties with respect to its (bore) diameter (Tab.3) is shown in Fig.7. To account for the bearing housing's mass, the total bearing mass is incremented by an empirical housing factor of 80/27 (NLR (2026)).

275 The empirical bearing property database is supplemented in the bearing component at the class level, facilitating implementation of its partial derivatives with respect to the design variables (i.e.  $D$ ). The supplied partial derivatives are verified against the complex-step method - making sure the derivatives' float representations are not hindered by subtractive cancellation - thereby rendering gradients to machine-zero precision.

**Table 3.** Bearing property estimations with respect to its bore diameter ' $D$ ' – for heavy load cases; \* -code enhancements.

Name	Type	$D_{max}^{sample}$ [m]	Face width [m]*	Mass [m]	$C$ [kN]*	$\mathbf{r}^*$
CARB	Non-MR	1.4	$0.4299 D + 0.0382$	$3,682.8 D^{2.7676}$	$16,676.0 D^{1.4746}$	$[0, 1, 1, 0, 0, 0]$
CRB	Non-MR	1.8	$0.157 D + 0.0849$	$1,070.8 D^{1.8278}$	$4,526.5 D^{0.9556}$	$[0, 1, 1, 0, 0, 0]$
SRB	Non-MR	2	$0.2463 D + 0.185$	$2,688.3 D^{1.8877}$	$13,878.0 D^{1.0796}$	$[1, 1, 1, 0, 0, 0]$
TRB	MR	1.4	$0.1499 D$	$543.01 D^{1.9043}$	$1,993.8 D^{0.318}$	$[1, 1, 1, 0, 1, 1]$
TRB2*	MR	4	$0.1541 D + 0.2087$	$1,442.6 D^{1.8932}$	$6,579.9 D^{0.8592}$	$[1, 1, 1, 0, 1, 1]$

280 From the right plot in Fig.7, the high dynamical load capacity ( $C$ ) of CARB and SRB type bearings can be seen. More specifically, to reach  $C = 20\text{MN}$ , CARB must be only 1 m in diameter, compared to almost 4 m needed for a TRB2. This allows setups with CARB and SRB to satisfy the FLS-life constraint already at a lower diameter, or at lower masses, compared to setups with a TRB2. The discussion here revolves around only two objectives: minimum mass and a satisfied FLS-life constraint. In reality, practical implications such as axial displacements, bearing roller load distribution, MSA load paths and isolation from the gearbox, etc., govern the setup's failure rate and reliability.

### 2.3.2 Equivalent bearing loads (P)

285 Equivalent bearing loads can be calculated, according to ISO (2007), as in Eq.22.

$$\mathbf{P} = X\mathbf{F}_{rad} + Y\mathbf{F}_x \quad (22)$$

with the dynamic load factors ( $X$ ,  $Y$ ) from Tab.4.

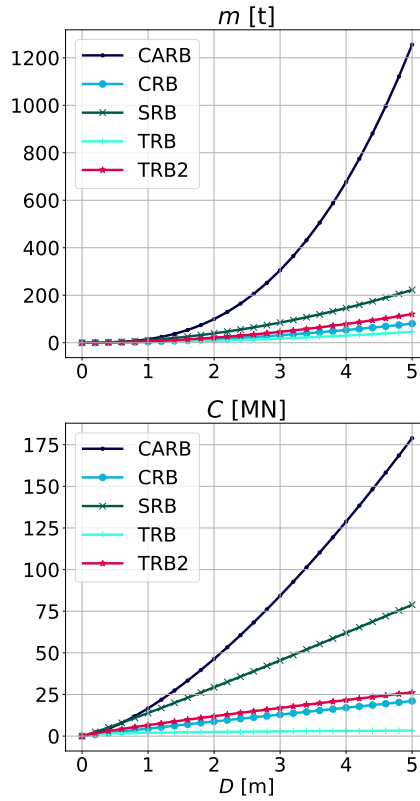


**Figure 7.** Bearing properties (mass and C) with respect to bearing bore diameter

**Table 4.** Dynamic load factor values (X,Y) for double-row radial roller bearings

	$F_{ax}/F_{rad} \leq e$	$F_{ax}/F_{rad} > e$
	<i>light, <math>(\cdot)_1</math></i>	<i>heavy, <math>(\cdot)_2</math></i>
X	1	0.67
Y	$0.45 \cot \alpha$	$0.67 \cot \alpha$

### 2.3.3 Weighted-averaged fatigue equivalent loads ( $P$ )

There are 2 ways to aggregate bearing equivalent load time series across all wind speeds " $\mathbf{P}$ " to a weighted-averaged scalar equivalent load " $P$ ", i.e.  $\mathbf{P} \rightarrow P$ , in order to formulate the bearing life constraint:

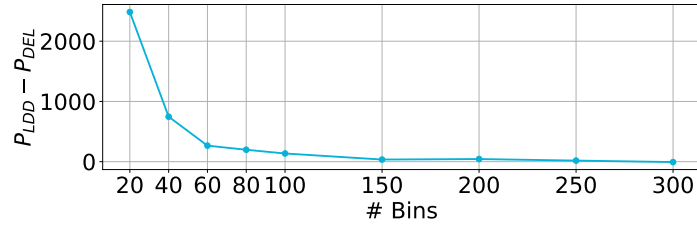


**Figure 8.** Comparing methods to aggregate bearing equivalent load time series: DEL and LDD

1. LRD (Load Revolution Distribution):

It is the conventional method of time-series histogram-bin counting of loads ( $\mathbf{P}$ ) and corresponding rotational speeds ( $\mathbf{\Omega}$ ); the reader is referred to the wind turbine standard IEC (2012) for more details on its computation.

295

2. DEL (Damage Equivalent Load):

The full raw time series of main bearing equivalent loads ( $\mathbf{P}$ ) is reduced into the fatigue relevant metric ‘DEL’. First, the vector of DEL for all wind speeds is calculated using Eq.23.

$$\mathbf{p}_{DEL} = \left( \frac{\sum_i (\mathbf{P}^p \odot \mathbf{N})}{\mathbf{n}} \right)^{1/p}; \quad \mathbf{N} = \frac{\mathbf{\Omega}}{60} \cdot \Delta t; \quad \mathbf{n} = \sum_i \mathbf{N} \quad (23)$$

300 where,  $\mathbf{\Omega} = \Omega_{i,j}$  is the matrix of rotational speeds for the entire DLC,  $\Delta t = t_2 - t_1$  is the (constant) time step,  $\mathbf{n}$  is total number of revolutions in the time series,  $\sum_i$  is sum-over-rows resulting in a vector of length  $n_{ws}$  (number of wind speeds), and  $\odot$  is element-wise (or Hadamard) product of two matrices.

Furthermore,  $\mathbf{p}_{DEL}$  is weighted by the wind speed probability  $\mathbf{p}_u$  and combined into a single aggregate fatigue metric:

$$P_{DEL} = \left( \sum_J (\mathbf{p}_{DEL}^p \odot \mathbf{p}_u) \right)^{1/p} \quad (24)$$

305 A validation of the analytical method of DEL shows that it corresponds to the converging value of an equivalent bin-counting LDD algorithm, Fig.8. This can also be understood when one sees the DEL-formulation counting the bins with bin-width being the (simulation) time step ( $\Delta t$ ) or the number of bins being the total number of (simulation) time steps ( $(\sum j) - 1 = 72\,000 - 1$ ).



### 2.3.4 Fatigue life equation ( $L_{10}$ )

310 It can be calculated, according to ISO (2007), as in Eq.25.

$$L_{10,rev} = \left(\frac{C}{P}\right)^p \cdot 10^6$$

$$p \text{ (fatigue exponent)} = \begin{cases} \frac{10}{3} & \text{: roller bearing} \\ 3 & \text{: ball bearing} \end{cases} \quad (25)$$

$$L_{10,hrs} = \frac{L_{10,rev}}{n_0 \cdot 60}$$

where  $n_0$  [rpm] is the rated rotational speed of the rotor/main shaft.

Future work entails utilizing ( $a_{ISO} a_e$ ) for the modified life equation ( $L_{nm}$ ), Ishihara et al. (2025).

315 The  $L_{10}$ -life in WTMBs is based on certain assumptions (Hart et al. (2020)), from them being: 1. Condition of elasto-hydrodynamic lubrication (EHL) is satisfied throughout the bearing lifetime, 2. Steady-state operation, i.e. not taking into account intermittent operational conditions, 3. Presence of wear instead of, or alongside rolling contact fatigue (RCF) is not accounted for.

320 The 2 methods of LRD and DEL render two ways to calculate bearing life:

LRD based:

$$L_{10,rev}^{LRD} = \left(\frac{C}{P_{LRD}}\right)^p \cdot 10^6 \quad (26)$$

DEL based:

325 
$$L_{10,rev}^{DEL} = \left(\frac{C}{P_{DEL}}\right)^p \cdot 10^6 \quad (27)$$

In light of efficient optimization of fatigue-driven components, utilizing full time-series non-smooth bin-counting (Eq.26) is shown in (Gupta and Nejad (2026)) to render convergence issues. Instead analytical DEL-based fatigue-life constraints (Eq.27) render efficient and robust optimization.

## 2.4 Shaft Structural Model

330 Conventional models define the main-shaft ULS criterion using low-fidelity analytical formulations (Guo et al. (2015b), Eq.(2.19-20)) to calculate loads (forces and moments) and subsequent (von-Mises) stresses in the main-shaft elements (Budy-nas et al. (2021), Eq.5-15).

In this study, a more structurally sound and physically consistent stiffness-based shaft structural model is utilized for the LSS ULS constraints formulation, numerically implemented in WISDEM using the mid-fidelity `Frame3DD` library, and based



335 on the stress formulation in Appendix Sect.C). The LSS is modelled with Timoshenko beam elements and includes shear deformation and geometrical stiffness effects. The model enhances design accuracy and setup validity, matching real drivetrain physics better compared to the the low-fidelity analytical equations.

With reference to the present moment-reacting-MB2 MSA setup, a statically indeterminate system is created, which can not be solved using only static equilibrium equations and (bearing) stiffness must be taken into account. The structural solver  
340 `pyFrame3DD` advantageously handles and solves such models through stiffness-deformation compatibility (direct stiffness and mass assembly) that replaces equilibrium.

### 3 Constraint Gradient-based Optimization

#### 3.1 Overview

The constraint gradient-based optimization problem with a single objective can be formulated as in Eq.28.

345 
$$\text{find } \mathbf{d}^* \tag{28}$$

which minimizes  $f(\mathbf{d})$

subjected to  $\mathbf{g}(\mathbf{d}) < 0$

$\mathbf{h}(\mathbf{d}) = 0$

$\mathbf{d} \in [\mathbf{d}^{\text{lb}}, \mathbf{d}^{\text{ub}}]$

350 where  $f$  is the objective function, and ‘lb’ and ‘ub’ represent the lower and upper bounds, respectively.

**Table 5.** Optimization driver options

Optimizer option	Value
Optimizer	SLSQP
Tolerance	$10^{-6}$
Maximum iterations	20

An eXtended Design Structure Matrix (XD<sub>SM</sub>) diagram, describing the flow of data variables and sequence of module (drivetrain component) execution, of the present multidisciplinary optimization problem, is shown in Fig.9.

#### 3.2 Objective function ( $f$ )

355 The present work investigates weight-optimization of critical drivetrain components while preserving critical bearing fatigue metrics.

Barter et al. (2023) analysed 30 large (15 – 25MW) FOWT DT concepts numerically (using NLR’s WEIS) and concluded that, unlike fixed-bottom WTs that showed relatively flatter mass-LCOE landscape, floating concepts showed greater depen-

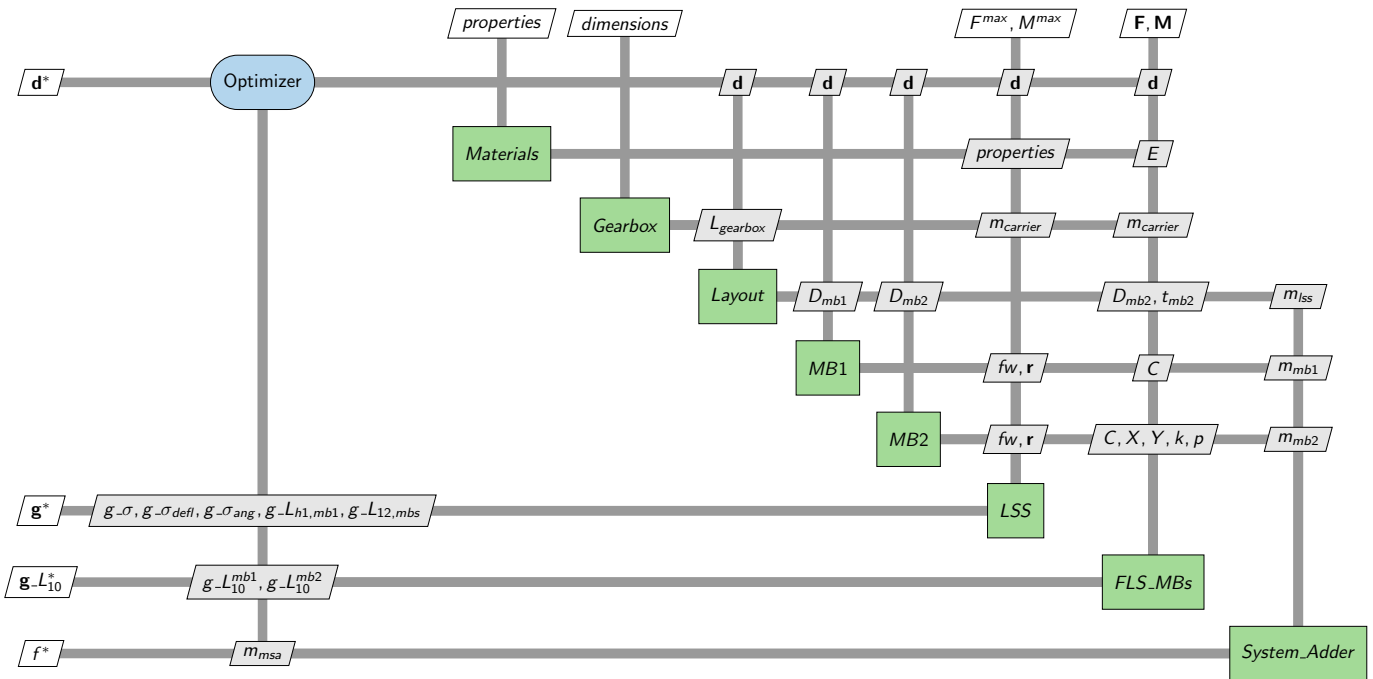


**Figure 9.** XDSM diagram of the main-shaft assembly optimization problem

360 dependency on and benefit with a lighter rotor-nacelle assembly (RNA). It is concluded that the impact of an optimal drivetrain design is threefold: (1) Tower-top mass and inertial loads contribute towards support-structure design, (2) Weight-based cost contributions to turbine CapEx in LCOE, and (3) Contribution to overall electro-mechanical reliability and efficiency.

Therefore, the primary objective is to minimize the mass of the main shaft assembly, which includes the low-speed shaft (LSS) and the two MBs:  $f = (m_{MSA} + m_{mb1} + m_{mb2})$ .

### 3.3 Design Variables (d)

The design variables used are listed in Tab.6, and are those marked red in Fig.10.

**Table 6.** Design variables for MSA design optimization

d	symbol	type	lb	ub	[units] description
$d_1$	$L_{h1}$	float	0.1	5.0	[m] distance between hub-LSS input and MB1
$d_2$	$L_{12}$	float	0.1	8.0	[m] distance between MB1 and MB2
$d_3$	$D_{lss}$	array[2]	1.0	5.0	[m] diameters of LSS shaft ends
$d_4$	$t_{lss}$	array[2]	$4 \cdot 10^{-3}$	0.5	[m] thicknesses of LSS shaft ends

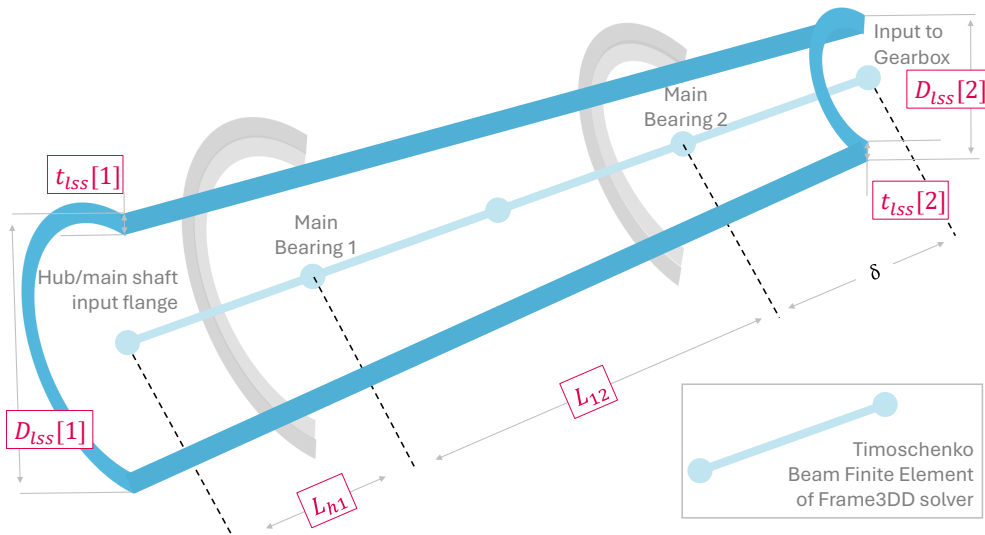


**Figure 10.** Design variables of the main-shaft assembly

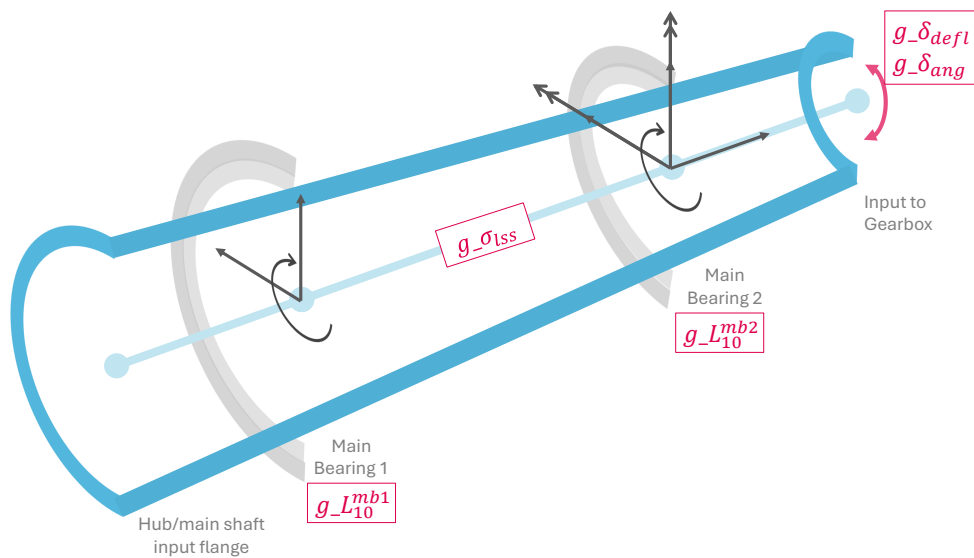


**Figure 11.** Inequality constraints on the main-shaft assembly



**Table 7.** Constraints for LSS design optimization;

(Abbreviations: DW = downwind, GB = gearbox, DT = drivetrain, TT = tower-top).

<b>g(d)</b>	<b>symbol</b>	<b>type</b>	<b>bound</b>	<b>description</b>
$g_1$	$\sigma_{lss}$	array[4]	$\leq 1.0$	ratio of von-Mises stresses in shaft elements to that permissible (Eq.C3)
$g_2$	$\delta_{defl}$	float	$\leq 1.0$	ratio of deflection at the LSS-end (GB input) to maximum permissible ( $\delta_{defl, max}$ )
$g_3$	$\delta_{ang}$	float	$\leq 1.0$	ratio of angular deflection at the LSS-end (GB input) to maximum permissible ( $\delta_{ang, max}$ )
$g_4$	$L_{h1, mb1}$	float	$\geq 0.0$	$L_{h1}$ should be greater than half of MB1 face width
$g_5$	$L_{12, mbs}$	float	$\geq 0.0$	$L_{12}$ should be greater than half of the sum of MB face widths
$g_6$	$L_{10}^{mb1}$	float	$\geq 1.0$	$L_{10}$ -life of MB1 should be more than design life
$g_7$	$L_{10}^{mb2}$	float	$\geq 1.0$	$L_{10}$ -life of MB2 should be more than design life

### 365 3.4 Inequality Constraints (g)

The constraints used are listed in Tab.7, and are those marked red in Fig.11. The von-Mises stress constraint is calculated as in Eq.29:

$$g_{\sigma_{lss}} = \frac{\gamma \cdot \sigma_v}{\sigma_{yield}} \quad (29)$$

where  $\sigma_v$  is the vector of von-Mises stresses in each discretized element of the LSS (Eq.C3) and  $\gamma = \gamma_f \cdot \gamma_n \cdot \gamma_m$ , the total partial safety factor (SF), Tab.B1.

The MB FLS life constraint can be defined as in Eq.30, where the  $L_{10}$ -life of the main bearings ( $L_{10}^{mb*}$ ) should exceed the total design life of the bearing or the wind turbine.

$$g_{L_{10}^{mb*}} = \left( \frac{L_{10, hrs}}{L_{design, hrs}} \right)^{1/p} = \left( \frac{L_{10, hrs}}{L_{design, yrs} \cdot 8766} \right)^{1/p} \quad (30)$$

## 375 4 Discussion of Results

### 4.1 Analytical moment-reacting MSA model

To verify the analytical formulation, an equivalent mid-fidelity beam finite-element model of the main-bearing-shaft assembly was created using the pyFrame3DD structural model, with nodes, forces and reactions as shown in Fig.2.

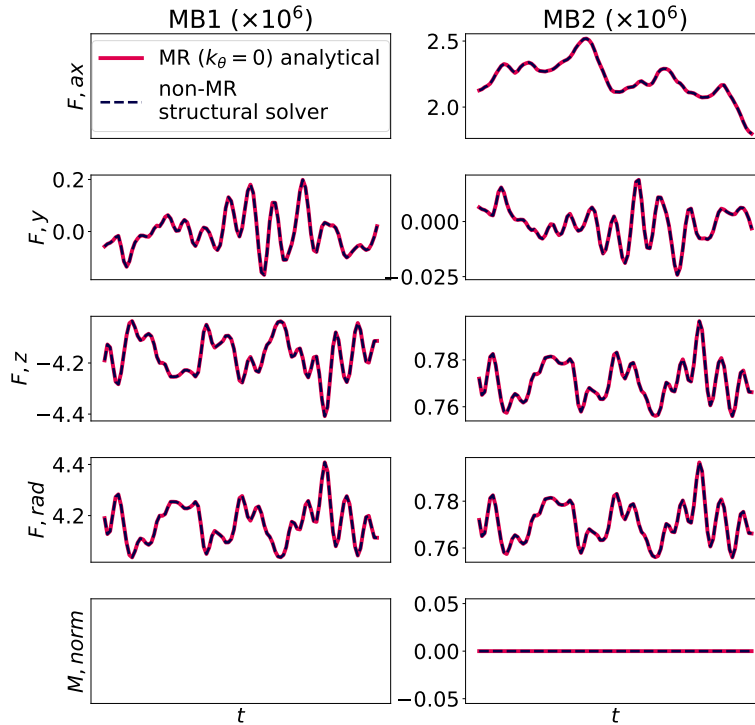


**Figure 12.** Non-moment-reacting MB2: comparing bearing reactions from the structural solver and the analytical EB-beam formulation (with  $k_\theta = 0$ )

### 380 Non-moment reacting (non-MR) MB2

With the limiting case of  $k_\theta = 0$ , as defined in Sect.2.2.2, the conventional non-moment reacting MB2 setup is rendered (Eqs.1, 2), which is illustrated in Fig.12.

### Moment-reacting (MR) MB2

385 With MB2 now reacting to moments ( $k_\theta \neq 0$ ), Fig.13 compares the bearing reactions between the mid-fidelity structural solver and the proposed EB-beam-based formulation from Sect.2.2.3.

Tab.8 lists the maximum absolute percentage (MAP) error (Eq.D1) for the different main bearing reactions, where  $M_{norm}^{mb2} = \sqrt{(M_y^{mb2})^2 + (M_z^{mb2})^2}$ .



**Table 8.** Error on MR bearing loads between structural solver and analytical EB-beam formulation; corresponding to Fig.13

Reaction	% Error (MAPE)
$F_{rad}^{mb1}$	0.024
$F_{ax}^{mb2}$	0.0
$F_{rad}^{mb2}$	0.213
$M_{norm}^{mb2}$	0.28

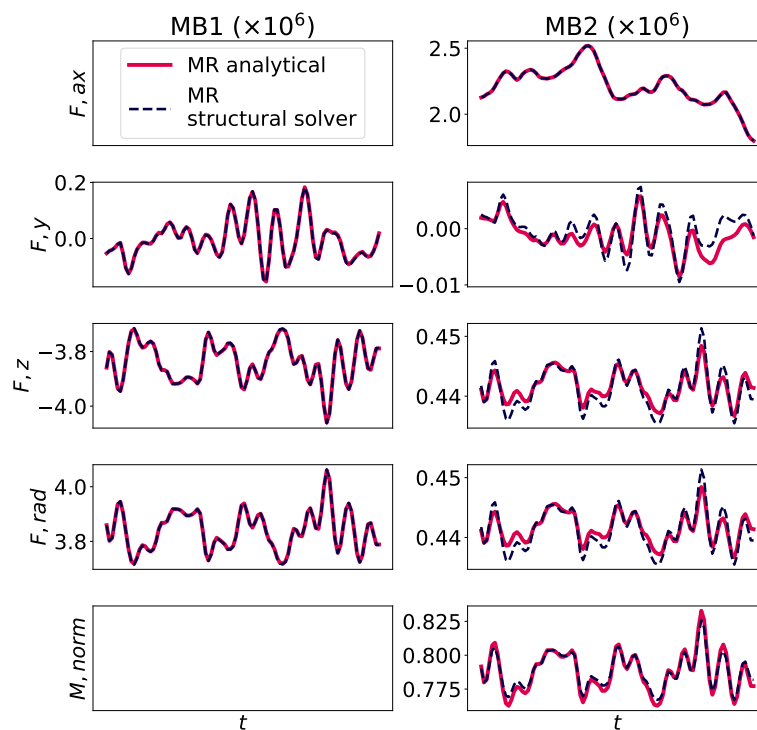


**Figure 13.** Moment-reacting MB2: comparing bearing reactions from the structural solver and the proposed analytical EB-beam formulation (with  $k_\theta \neq 0$ )



## 390 4.2 Design Optimization of the Main-Shaft Assembly

### 4.2.1 Variable convergence and limit-state comparison

MSA design variable optimization convergence is shown in Fig.14, while the optimal design is listed in Tab.9. To converge from a given set of initial conditions far from the minima, the design optimization of 6 design variables under 7 constraints took  $\approx 15$  s, 16 iterations, 19 function evaluations and 16 gradient evaluations. At the optimal design, all constraints are satisfied, while the shaft stress and bearing fatigue-life constraints are active.

**Table 9.** Results from MSA design optimization; (\*)-only evaluated, not included in optimization.

$d, g, f$	Converged value	
	ULS only	ULS+FLS
$L_{h1}$	0.149	0.310
$L_{12}$	0.354	1.721
$D_{lss}$	[1.438, 1.284]	[3.440, 3.204]
$t_{lss}$	[0.004, 0.510]	[0.087, 0.082]
$\max(g(\sigma_{lss}))$	1.0	0.99
$g(L_{10}^{mb1})$	(0.041)*	1.0
$g(L_{10}^{mb2})$	(0.055)*	1.0
$m_{MSA}$	23 095	110 409

395

According to IEC (2012) (61400-4), the MBs should exceed a life of 100 000 hours for a design lifetime of 20 years, and the former (life in hours) should be adjusted for a different design lifetime, e.g. 219150 hours for 25 years lifetime.

It can be noted from Tab.9 that considering only ULS constraints for mass minimization, as currently present in `DrivetrainSE` used to design the IEA 15MW turbine and drivetrain, does not render a reliable design in terms of critical bearing fatigue, wherein the evaluated  $L_{10}$ -life in hours was only 5.3 and 13.9 for MB1 and MB2 respectively, compared to 219150.0 hours  
 400 where the constraints are augmented with fatigue-life constraints for each bearing. This in turn shows that these type of machines are highly and critically driven by fatigue, negligence of which results in severe under-design.

### 4.2.2 Advantage of analytically-differentiable bearing fatigue formulation

Multiple sets of initial conditions (ICs) were chosen to showcase their effect on optimization convergence, as listed in Tab.10.

405  $L_{h1}$  and  $L_{12}$  (segment lengths of the main shaft) are varied, on a grid between their bounds.

Formulating the bearing fatigue constraint through DELs (Eq. 24) is considered, which are:

1. Smooth and analytically differentiable: analytical gradients are critical for convergence of gradient-based optimizers.

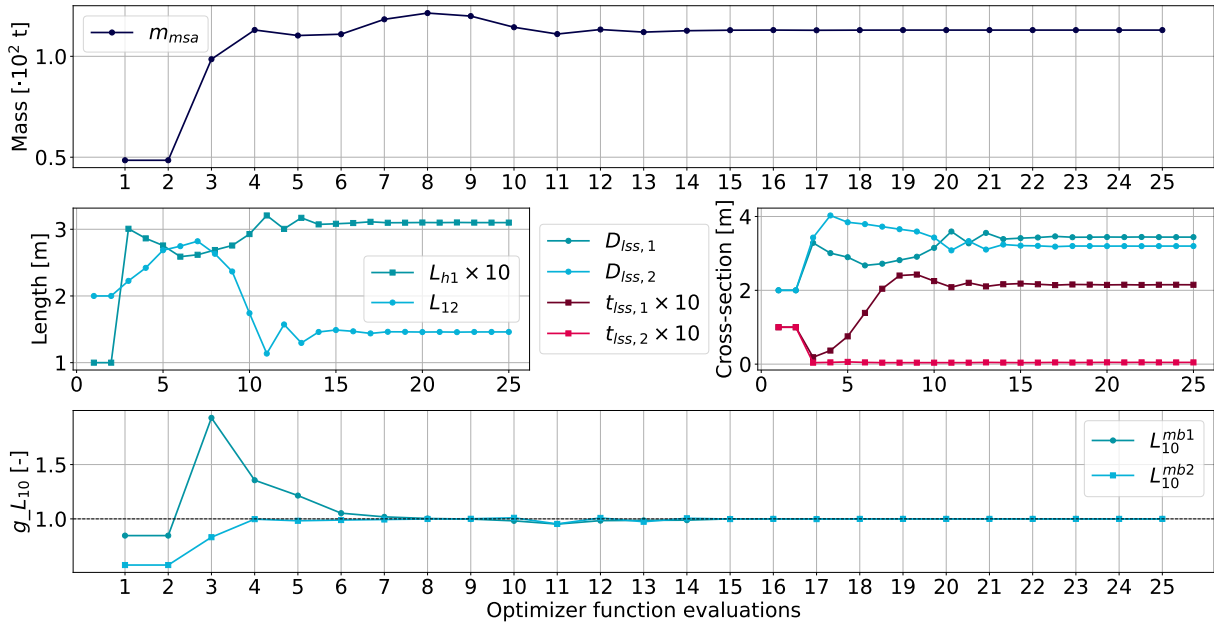


**Figure 14.** Convergence plot of optimization variables with iterations

**Table 10.** Initial conditions (ICs)

<i>d</i> / Set	1	2	3	4
$L_{h1}$	1.25	3.75	1.25	3.75
$L_{12}$	2.0	2.0	6.0	6.0

2. Computationally cheap: avoiding full DLC time-series histogram-bin-counting within the optimization loop.

By using smooth DEL constraints, the robustness within optimization is evident (Fig.15) by the consistent convergence  
 410 irrespective of widely different initial conditions – an indicator of potentially finding a global minimum.

### 4.2.3 Parametric study on viable main-bearing setups

Potentially viable main bearing combinations were varied between sets defined in Tab.11, their performance trade-offs were accessed and the converged design values were recorded; all other design variables and input parameters were kept unchanged.

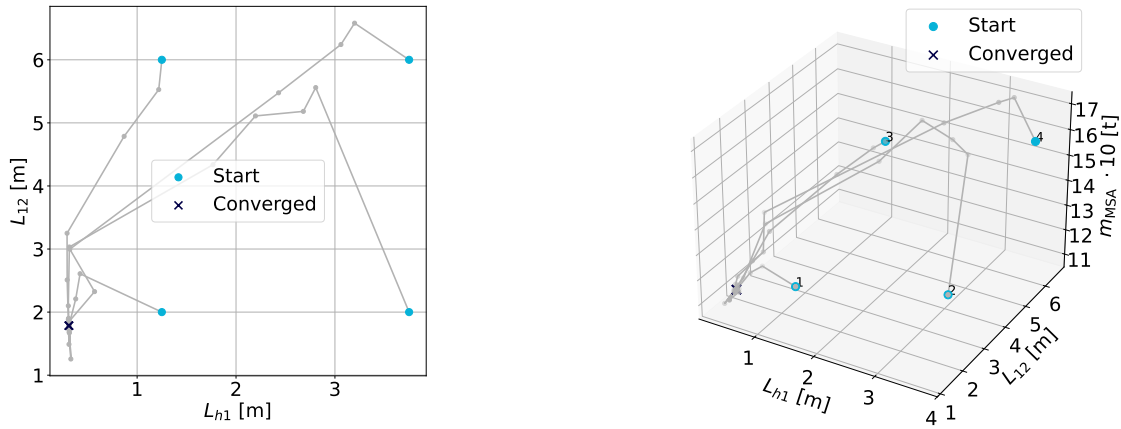


**Figure 15.** Smooth DEL-based constraint: optimization path and robust convergence.

**Table 11.** Design optimization on different main bearing configurations

-	Moment-reacting setups		Non-moment-reacting setups	
$d, g, f$	Set 1	Set 2	Set 3	Set 4
-	CRB+TRB2	CARB+TRB2	CRB+SRB	CARB+SRB
$L_{h1}$	0.310	0.438	0.314	0.449
$L_{12}$	1.721	2.153	3.077	2.623
$D_{lss}$	[3.440,3.204]	[1.686,3.552]	[3.681,1.021]	[2.046,1.699]
$t_{lss}$	[0.087,0.082]	[0.466,0.004]	[0.059,0.428]	[0.5, 0.5]
$g_{\sigma_{lss}}$	[0.26,0.99,0.99,0.76]	[0.45,0.80,0.80,1.0]	[1.0,1.0,1.0,0.81]	[0.33,0.86,1.0,0.71]
$g_{\delta_{ang}}$	0.0	0.0	0.282	0.283
$g_{\delta_{defl}}$	0.003	0.003	0.99	0.99
$g_{L_{10}^{mb1}}$	1.0	3.05	1.0	2.945
$g_{L_{10}^{mb2}}$	1.0	1.0	1.06	1.349
$m_{mb1}$	39 977	92 867	41 167	99 742
$m_{mb2}$	53 281	53 267	19 122	30 578
$m_{lss}$	17 151	34 692	38 119	60 492
$f$	110 409	180 828	98 409	190 813

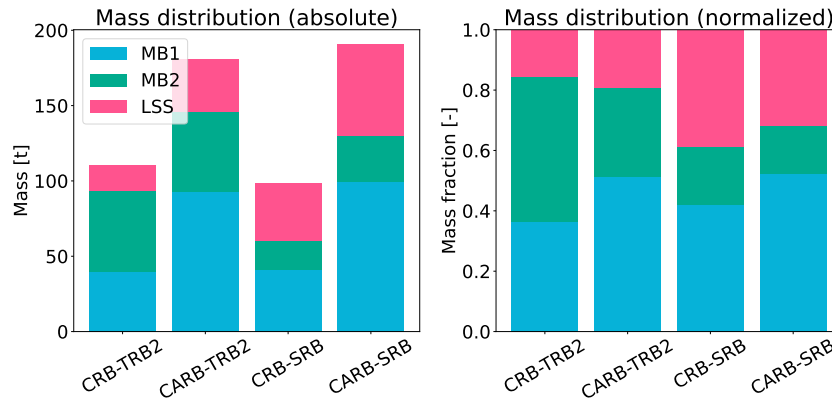


**Figure 16.** System mass distribution across different main-bearing configuration setups

415 The optimization results demonstrate a strong dependency of the drivetrain system mass on the main bearing configuration and load transfer mechanism.

**System component mass distribution, Fig.16:**

420 The optimized mass distribution reveals that the dominant contributor to total mass depends strongly on the bearing configuration.

The lowest total system mass (98 t) is achieved for the CRB+SRB configuration, approximately 48% reduction compared to the heaviest CARB+SRB design. Mass-efficiency is attributed to the relatively high dynamic load capacity of SRB at low bearing masses.

425 CARB-based configurations consistently result in significantly higher total mass ( $\approx 180 - 190 t$ ). This behaviour is attributed to the bearing's inherent heavy-weight property even at low diameters. On the other hand, CRB-based solutions enable a more balanced mass allocation between bearings and the shaft.

Moment-reacting (TRB2-based) systems exhibit reduced shaft mass due to internal moment support within the bearing arrangement. However, this advantage is slightly offset by increased bearing mass, due to the need for higher bearing capacity, leading to marginally sub-optimal total system mass compared to the optimally lightest configuration.

430

**Non-linear constraint utilization heatmap, Fig.17:**

The constraint utilizations are shown as a heatmap across different bearing configurations, where a black dot highlights active constraints and red indicates values approaching unity. This enables direct identification of governing constraints in each design optimization.

435 Investigating what drives the design and guides it to convergence, it can be seen that the ultimate shaft stresses are active ( $\max(g_{\sigma_{lss}}) \approx 1$ ) in both MSA setup configurations. However, differences are seen when the bearing fatigue-life ( $g_{L_{10}}$ )

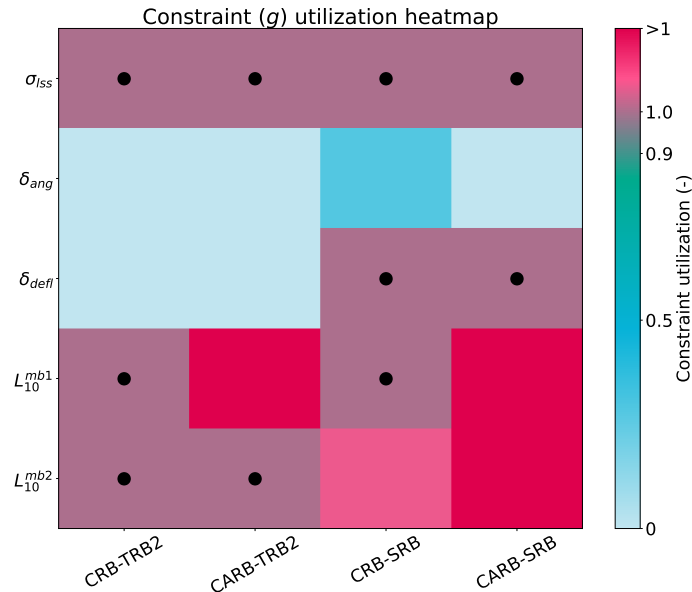


**Figure 17.** Constraint activity heatmap of design optimization across different main-bearing configuration setups

and LSS end-deflections ( $g_{\delta_{defl}}$ ) are monitored. For MR setups, the fatigue lives are the design drivers. For non-MR setups on the other hand, the shaft deflections seem to in addition dictate the design. This can be related to the incapability of MB2 to react to tilting moments/NTLs, increasing bearing (axial and radial) loads and shaft loads (peaks and those carried through to  
 440 GB-input), consequently, increasing the shaft end-deflection.

**Trade-off comparison of total system mass and maximum constraint, Fig.18:**

The Pareto plot demonstrates that CARB-based configurations are structurally inefficient, as they require significantly higher mass while still operating under active constraints. In contrast, CRB-based configurations achieve near-optimal constraint uti-  
 445 lization at substantially lower system mass.

**Geometric design variable comparison, Fig.19:**

To enables direct interpretation of how each design variables (geometric parameter) responds to changes in bearing configuration, each geometric parameter is presented in an individual subplot, and colours indicate different bearing arrangements.  
 450 The figure highlights how bearing-combination choices influences shaft geometry, particularly diameter and wall thickness, reflecting different load transfer mechanisms.

Non-MR setups are seen to converge to a higher bearing span distance  $L_{12}$ . This is because they result in higher bearing forces (Eqs.1, 2, and Fig.5) which the model tries to lower by increasing the span distance, being inversely related to the bearing forces. Consequently, the LSS masses ( $m_{lss}$ ) in non-MR setups are more than MR setups. On the other hand, MR-

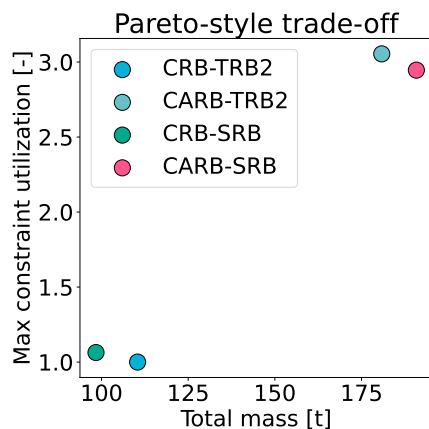


**Figure 18.** Pareto-style trade-off comparison of total system mass and maximum constraint for different main bearing configurations

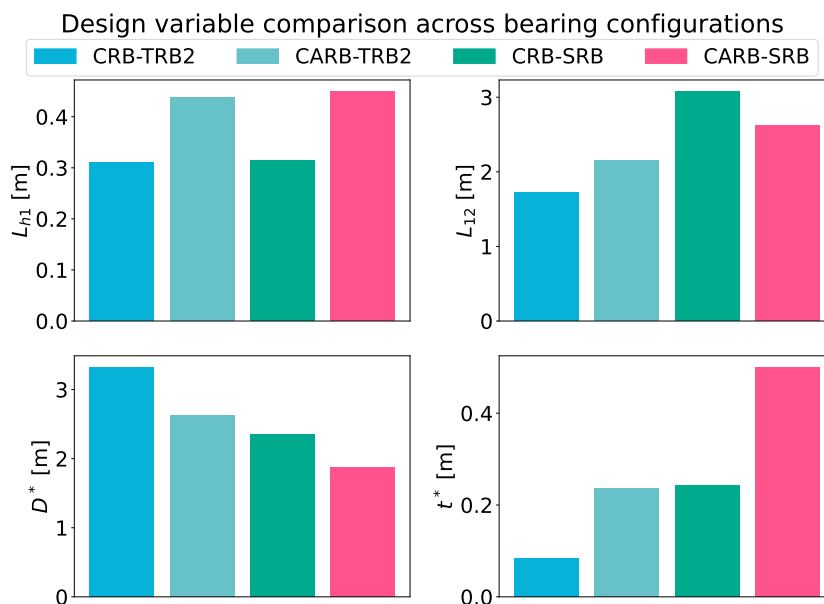


**Figure 19.** Comparison of optimized design variables for different main bearing configurations; (\*) indicates mean values.



455 systems (TRB2-based) exhibit reduced LSS mass due to internal moment support by the MR bearing arrangement, hence relieving shaft loads.

## 5 Conclusions

In light of efficient system-level multi-disciplinary optimization (MDAO) of floating offshore wind turbines, the paper highlights the lack of integration of and details in drivetrain design found in the current state-of-the-art, the significance and need for  
460 coupled, reliable and fatigue-driven drivetrain modelling, and proposes to fill this gap through efficient multi-fidelity constraint gradient-based optimization, enhancing NLR's WISDEM-WEIS MDAO frameworks.

As a numerical example, the drivetrain components first in line in the load path from the rotor blades, i.e. the main bearing-shaft assembly is optimized for minimum mass (or maximum power-density). The criticality of fatigue in large wind turbine drivetrains as a design driver and the importance of including FLS bearing life constraints over only-ULS static structural  
465 constraints are shown, Tab.9.

Moment-reacting MB2 is shown to showcase a few benefits such as:

1. Redistributes bearing loads, lowering MB1 and MB2 radial forces (Fig.4)
2. Ignoring MB2 moments would under-predict MB2 stiffness effects and over-predict MB1 loads
3. Reduces peak shaft bending stresses (Tab.11)
- 470 4. Consistency between bearing physics, statics, and the structural solver
5. Gradient sensitivities are damped as moments are redistributed via stiffness

Moreover, DLC load spectra reduction is seen in the light of efficient gradient-based design optimization, wherein conventional non-smooth histogram-bin-counting (LRD) is replaced with analytically-differentiable damage equivalent loads (DEL) giving consistent results with robust convergence, Tab.12.

475 The proposed and enhanced setup allowed efficient exploration of various viable main-bearing configurations and the design driving differences between moment-reacting and non-moment-reacting bearing supports was shown.

The optimization demonstrates that the selected main-bearing arrangement has a significant influence on the component masses, dominant contributor to total mass, and load distribution of the main-bearing-shaft system. The constraint activity analysis further highlights the governing design mechanisms. Designs with active bearing life constraints indicate that bearing  
480 fatigue performance limits further mass reduction, whereas shaft stress and deflection constraints govern configurations where bearing loads are alleviated.

Lastly, the optimal drivetrain configuration is governed by how effectively moment and axial loads are distributed between bearings and shaft to satisfy ultimate and fatigue-critical metrics, rather than purely by component sizing.



In conclusion, the present work innovates on the current state-of-the-art in MDAO for wind turbine drivetrains, enhancing  
485 its detailed design and combining structural dynamics with critical fatigue-driven metrics, and is geared for further integration  
into system-level coupled wind turbine analysis and optimization.

**Table 12.** Summary: GBO behaviour vs.FLS-load reduction method; *Abbreviations:* FD-finite difference, AG-analytical gradients.

Approach	Gradient Quality	GBO Behavior
LRD + FD	Noisy, discontinuous	Inconsistent convergence/failure
LRD + AG	Not possible (not differentiable)	-
Smooth DEL + FD	Sufficient	Converges reliably
Smooth DEL + AG	Exact	Faster, robust and efficient convergence

## 5.1 Future work

Future work aims to include more accurate and detailed bearing life calculations (TS 16281 ISO (2025)), analytical derivatives  
for bearing FLS constraints and illustrating optimization efficiency improvements due to it. Moreover, work is on-going in  
490 incorporating detailed main-bearing-shaft assembly and gearbox models within state-of-art floating wind MDAO toolsets –  
steady-state (WISDEM) and transient control co-design (WEIS), and reporting innovations compared to the IEA-15MW refer-  
ence floating wind turbine.

*Code availability.* The methodology has been closely integrated into the open-source WISDEM WT-MDAO framework from NLR (2026),  
its drivetrain `DrivetrainSE`, the integrated wind turbine modules `WindPark`, and `.yaml` input file schemas are updated to compliment  
495 the enhancements. The code is available at the main author's `github` repository. Alongside this, the work also led to several source-code  
corrections in the framework's main repository.



## Appendix A: Site-Specific Environmental Conditions

Two offshore wind site locations are considered as part of the project – Utsira-Nord, Norway and Calabira, Italy. The environmental conditions (ECs) representative of the former site (Utsira-Nord) are selected for the drivetrain design optimization as they are harsher and more severe than the latter’s (Calabria), resulting in a more conservative and reliable design, applicable to  
505 both sites. For more details, the reader is referred to Made4Wind project’s Deliverable 2.1 ‘Use case scenario’ & Deliverable 5.1 Release 2.

## Appendix B: Wind Turbine Specifications

The wind turbine definition, relevant for inference of this study are defined, such as turbine and drivetrain parameters Tab.B1 and materials data Tab.B2.

510

In Tab.B1, the drivetrain properties are kept constant throughout the design optimization process but can be included as design variables. Moreover,  $\gamma_n$ , the partial safety factor for the consequence of failure facilitates adjustment of the reliability level which depends on the consequence of failure (DNV-ST-0437:2024 DNV (2024), Sect.2.5.2).

515 In Tab.B2,  $\sigma_{yield}$  is the ultimate yield and  $\sigma_{tensile}$  the ultimate tensile strength.

## Appendix C: Stress Utilization Equations

Forces and moments in each (beam) element ( $F$ ,  $M$ ) are calculated using the structural analysis tool, are used to calculate the von-Mises stress, and further formulate the stress utilization constraint.

Herein, for a circular cross-section (eg. tube), some shorthands can be written, differentiating the axial and shear components:

520 – Bending modulus  $S := I_y/R = I_z/R$

– Torsional shear constant  $C := I_x/R$

where  $I$  is the area moment of inertia, Tab.C1.

Axial stresses:

$$M = \sqrt{M_y^2 + M_z^2}$$
$$525 \sigma_{axial} = \sigma_a := \frac{|F_x|}{A} + \frac{M}{S} \quad (C1)$$

Shear stresses:

$$F = \sqrt{F_y^2 + F_z^2}$$
$$\sigma_{shear} = \tau := \frac{2 \cdot F}{A_s} + \frac{|M_x|}{C} \quad (C2)$$



**Table B1.** Wind Turbine Definition; <sup>(1)</sup>-defined in IEC (2019).

Property	Value [units]	Symbol	Description
Machine rating	15 [MW]	-	-
Upwind	True	-	-
Rated RPM	7.56 [rpm]	$n_0$	Rotor/main shaft rated rotational speed, in region-3
Rated torque	21.03 [MNm]	-	-
Lifetime	25 [years]	$L_{design,yrs}$	-
Tilt	6 [deg]	$\phi$	Drivetrain main shaft tilt
Drive height	5.614 [m]	$H_{drive}$	Vertical distance between the hub center and tower-top center
Overhang	12.0313 [m]	$L_{overhang}$	Horizontal distance between the hub center and tower-top center
Gear-ratio	49.6 [-]	-	-
Gearbox mass	138.73 [t]	-	-
Carrier mass	27.745 [t]	$m_{carrier}$	20% of the gearbox mass
Allowable LSS deflection	$10^{-4}$ [m]	$\delta_{defl,max}$	Maximum allowable deflection at the LSS-end or GB-input
Allowable LSS deflection	$10^{-3}$ [deg]	$\delta_{ang,max}$	Maximum allowable angular deflection at the LSS-end or GB-input
Tower-top diameter	6.5 [m]	-	-
Partial safety factor (SF)	1.35	$\gamma_f$	Partial SF <sup>(1)</sup> for loads
Partial SF	1.3	$\gamma_m$	Partial SF for material resistance
Partial SF	1.0	$\gamma_n$	Partial SF for consequence of failure

**Table B2.** Steel material defined for LSS drivetrain components; The full database can be found in MatWeb.

Properties	Value
$E (\times 10^9)$	205
$G (\times 10^9)$	80
$\rho$	7850.0
$\sigma_{tensile} (\times 10^6)$	814
$\sigma_{yield} (\times 10^6)$	485

where, for each beam element,  $F_x$  is the axial internal force,  $F_y$ ,  $F_z$  are shear forces,  $M_x$ ,  $M_y$ ,  $M_z$  are moments (torque and bending),  $A$  is the cross-sectional area, and  $A_s$  is the shear area.



**Table C1.** Area moment of inertia of a ring: cross-section of the main-shaft;

$$D_o = D_{lss}, D_i = (D_{lss} - 2 \cdot t_{lss})$$

Shape	$I$
Ring, through its diameter	$I_y, I_z = \frac{\pi(D_o^4 - D_i^4)}{64}$
Ring, through its centre	$I_x = 2 \cdot I_y$

Thereupon, the von-Mises stress (utilization) can be calculated as (Budynas et al. (2021)):

$$\sigma_v := \sqrt{\sigma_a^2 + \sigma_h^2 - (\sigma_a \cdot \sigma_h) + 3\tau^2} \quad (C3)$$

where,  $\sigma_h$  is the hoop stress.

## 535 Appendix D: Miscellaneous

### D1 Error Functions

In the following,  $\mathbf{y} = [y_i]$  and  $\hat{\mathbf{y}} = [\hat{y}_i]$  are data point vectors (of equal length =  $n$ ) corresponding to the true value and the predicted value respectively.

540 **MAPE (Mean Absolute Percentage Error)** is defined as:

$$\text{MAPE} = \frac{1}{n} \sum_{i=1}^n \left| \left( \frac{y_i - \hat{y}_i}{y_i} \right) \cdot 100 \right| \quad (D1)$$

*Author contributions.* **Vasudev Gupta:** Conceptualization, Data curation, Formal analysis, Investigation, Methodology, Project administration, Resources, Software, Validation, Visualization, Writing (original draft preparation and editing); **Amir R. Nejad:** Funding acquisition, Project administration, Supervision, Writing (review).

545 *Competing interests.* The co-author Amir R. Nejad is a member of the editorial board of the Wind Energy Science (WES) journal.



*Acknowledgements.* The authors acknowledge the financial support from the European Commission under the Horizon Europe framework programme through the Made4Wind project (no. 101136096). Moreover, generative artificial intelligence (AI) and large language model (LLM) open-access tools were used as general assistants in tasks such as coding, mathematics, writing and presentation.



## 550 References

- ISO 281:2007: Rolling bearings — Dynamic load ratings and rating life, International Organization for Standardization, 2007.
- IEC 61400-4: Design requirements for wind turbine gearboxes, 2012.
- DNVGL-ST-0437: Loads and site conditions for wind turbines, 2016.
- IEC 61400-1:2019: Wind energy generation systems - Part 1: Design requirements, International Electrotechnical Commission, 2019.
- 555 ISO 16281:2025: Rolling bearings — Methods for calculating the modified reference rating life for universally loaded rolling bearings, International Organization for Standardization, 2025.
- Allen, C., Viscelli, A., Dagher, H., Goupee, A., Gaertner, E., Abbas, N., Hall, M., and Barter, G.: Definition of the UMaine VoltumUS-S Reference Platform Developed for the IEA Wind 15-Megawatt Offshore Reference Wind Turbine, Tech. Rep. NREL/TP-5000-76773, 1660012, MainId:9434, <https://doi.org/10.2172/1660012>, 2020.
- 560 Barter, G. E., Sethuraman, L., Bortolotti, P., Keller, J., and Torrey, D. A.: Beyond 15 MW: A cost of energy perspective on the next generation of drivetrain technologies for offshore wind turbines, *Applied Energy*, 344, 121 272, <https://doi.org/https://doi.org/10.1016/j.apenergy.2023.121272>, 2023.
- Budynas, R. G., Nisbett, J. K., and Shigley, J. E.: *Shigley's mechanical engineering design*, McGraw-Hill, New York, NY, eleventh edition in si units edn., ISBN 978-0-07-717145-2, oCLC: 1226062640, 2021.
- 565 Chovan, C. and Fierro, A.: Improving Bearing Life in wind turbine main shafts and gearboxes, Timken, <https://www.timken.com/resources/timken-tdi-bearings-white-paper-improving-bearing-life-in-wind-turbine-main-shafts-and-gearboxes/>, 2021.
- Dao, C., Kazemtabrizi, B., and Crabtree, C.: Wind turbine reliability data review and impacts on levelised cost of energy, *Wind Energy*, 22, 1848–1871, <https://doi.org/10.1002/we.2404>, eprint: <https://onlinelibrary.wiley.com/doi/pdf/10.1002/we.2404>, 2019.
- DNV: DNV-ST-0437: Loads and site conditions for wind turbines, 2024.
- 570 Dykes, K., Damiani, R., Roberts, O., and Lantz, E.: Analysis of Ideal Towers for Tall Wind Applications, <https://doi.org/10.2514/6.2018-0999>.
- Gaertner, E., Rinker, J., Sethuraman, L., Zahle, F., Anderson, B., Barter, G. E., Abbas, N. J., Meng, F., Bortolotti, P., Skrzypinski, W., Scott, G. N., Feil, R., Bredmose, H., Dykes, K., Shields, M., Allen, C., and Viselli, A.: IEA Wind TCP Task 37: Definition of the IEA 15-Megawatt Offshore Reference Wind Turbine, <https://doi.org/10.2172/1603478>, 2020.
- 575 Guo, Y., Bergua, R., van Dam, J., Jove, J., and Campbell, J.: Improving wind turbine drivetrain designs to minimize the impacts of non-torque loads, *Wind Energy*, 18, 2199–2222, <https://doi.org/https://doi.org/10.1002/we.1815>, 2015a.
- Guo, Y., Parsons, T., King, R., Veers, P., and Dykes, K.: Analytical Formulation for Sizing and Estimating the Dimensions and Weight of Wind Turbine Hub and Drivetrain Components, <https://doi.org/10.2172/1215033>, 2015b.
- Guo, Y., Parsons, T., Dykes, K., and King, R.: A systems engineering analysis of three-point and four-point wind turbine drivetrain configurations, *Wind Energy*, 20, 537–550, <https://doi.org/10.1002/we.2022>, 2017.
- 580 Gupta, V. and Nejad, A. R.: Multi-fidelity gradient-based wind turbine main-shaft assembly optimization with analytical bearing fatigue, *Journal of Physics: Conference Series*, 3224, 052 023, <https://doi.org/10.1088/1742-6596/3224/5/052023>, 2026.
- Hart, E., Clarke, B., Nicholas, G., Kazemi Amiri, A., Stirling, J., Carroll, J., Dwyer-Joyce, R., McDonald, A., and Long, H.: A review of wind turbine main bearings: design, operation, modelling, damage mechanisms and fault detection, *Wind Energy Science*, 5, 105–124, <https://doi.org/10.5194/wes-5-105-2020>, 2020.
- 585



- Hart, E., Stock, A., Elderfield, G., Elliott, R., Brasseur, J., Keller, J., Guo, Y., and Song, W.: Impacts of wind field characteristics and non-steady deterministic wind events on time-varying main-bearing loads, *Wind Energy Science*, 7, 1209–1226, <https://doi.org/10.5194/wes-7-1209-2022>, 2022.
- Hart, E., Raby, K., Keller, J., Sheng, S., Long, H., Carroll, J., Brasseur, J., and Tough, F.: Main Bearing Replacement and Damage - A Field  
590 Data Study on 15 Gigawatts of Wind Energy Capacity, <https://doi.org/10.2172/1992019>, 2023.
- Ishihara, T., Wang, S., and Kikuchi, Y.: Fatigue prediction of wind turbine main bearing based on field measurement and three-dimensional elastic drivetrain model, *Engineering Failure Analysis*, 167, 108 985, <https://doi.org/10.1016/j.engfailanal.2024.108985>, 2025.
- Jasa, J., Bortolotti, P., Zalkind, D., and Barter, G.: Effectively using multifidelity optimization for wind turbine design, *Wind Energy Science*, 7, 991–1006, <https://doi.org/10.5194/wes-7-991-2022>, 2022.
- 595 Link, H., LaCava, W., Van Dam, J., McNiff, B., Sheng, S., Wallen, R., McDade, M., Lambert, S., Butterfield, S., and Oyague, F.: Gear-box Reliability Collaborative Project Report: Findings from Phase 1 and Phase 2 Testing, Tech. Rep. NREL/TP-5000-51885, 1018489, <https://doi.org/10.2172/1018489>, 2011.
- Liverud Krathe, V., Jonkman, J., Gebel, J., Rivera-Arreba, I., Nejad, A., and Bachynski-Polić, E.: Investigation of Main Bearing Fatigue Estimate Sensitivity to Synthetic Turbulence Models Using a Novel Drivetrain Model Implemented in OpenFAST, *Wind Energy*, 28,  
600 e70 005, <https://doi.org/10.1002/we.70005>, 2025.
- Martins, J. R. R. A. and Ning, A.: *Engineering Design Optimization*, Cambridge University Press, Cambridge, UK, ISBN 9781108833417, <https://doi.org/10.1017/9781108980647>, 2022.
- MatWeb: Material Property Data, <https://www.matweb.com/search/DataSheet.aspx?MatGUID=38108bfd64c44b4c9c6a02af78d5b6c6&ckck=1>.
- 605 Musial, W., Spitsen, P., Duffy, P., Beiter, P., Marquis, M., Hammond, R., and Shields, M.: Offshore Wind Market Report: 2022 Edition, Tech. rep., National Renewable Energy Lab. (NREL), Golden, CO (United States), <https://doi.org/10.2172/1883382>, 2022.
- Nejad, A. R.: Modelling and Analysis of Drivetrains in Offshore Wind Turbines, chap. 3, pp. 37–101, John Wiley Sons, Ltd, ISBN 9781119097808, <https://doi.org/https://doi.org/10.1002/9781119097808.ch3>, 2018.
- Nejad, A. R., Keller, J., Guo, Y., Sheng, S., Polinder, H., Watson, S., Dong, J., Qin, Z., Ebrahimi, A., Schelenz, R., Gutiérrez Guzmán,  
610 F., Cornel, D., Golafshan, R., Jacobs, G., Blockmans, B., Bosmans, J., Pluymers, B., Carroll, J., Koukoura, S., Hart, E., McDonald, A., Natarajan, A., Torsvik, J., Moghadam, F. K., Daems, P.-J., Verstraeten, T., Peeters, C., and Helsen, J.: Wind turbine drivetrains: state-of-the-art technologies and future development trends, *Wind Energy Science*, 7, 387–411, <https://doi.org/10.5194/wes-7-387-2022>, 2022.
- NLR: WISDEM, <https://github.com/WISDEM/WISDEM>, 2026.
- Patryniak, K., Collu, M., and Coraddu, A.: Multidisciplinary design analysis and optimisation frameworks for floating offshore wind turbines: State of the art review, *Ocean Engineering*, 251, 111 002, <https://doi.org/10.1016/j.oceaneng.2022.111002>, 2022.
- 615 Perez-Moreno, S. S., Zaaier, M. B., Bottasso, C. L., Dykes, K., Merz, K. O., Réthoré, P.-E., and Zahle, F.: Roadmap to the multidisciplinary design analysis and optimisation of wind energy systems, *Journal of Physics: Conference Series*, 753, 062011, <https://doi.org/10.1088/1742-6596/753/6/062011>, 2016.
- Sethuraman, L., Quick, J., Dykes, K., and Guo, Y.: Exploring Optimization Opportunities in Four-Point Suspension Wind Turbine Drivetrains through Integrated Design Approaches, <https://doi.org/10.2514/6.2018-1000>.
- 620 Stirling, J., Hart, E., and Kazemi Amiri, A.: Constructing fast and representative analytical models of wind turbine main bearings, *Wind Energy Science*, 6, 15–31, <https://doi.org/10.5194/wes-6-15-2021>, 2021.

<https://doi.org/10.5194/wes-2026-105>  
Preprint. Discussion started: 25 June 2026  
© Author(s) 2026. CC BY 4.0 License.



- Veers, P.: Wind Energy Modeling and Simulation - Volume 2: Turbine and System, The Institution of Engineering and Technology, <https://doi.org/10.1049/PBPO125G>, 2019.
- 625 Wenske, J.: Wind Turbine System Design. Volume 1, The Institution of Engineering and Technology, <https://doi.org/10.1049/PBPO142F>, 2022.